JACS
JOURNAL OF THE AMERICAN CHEMICAL SOCIETY
ARTICLE
pubs.acs.org/JACS

Perovskite, $LiNbO_3$, Corundum, and Hexagonal Polymorphs of $(In_{1-x}M_x)MO_3$

Alexei A. Belik,*[,†] Takao Furubayashi,[§] Hitoshi Yusa,[‡] and Eiji Takayama-Muromachi[†]

[†]International Center for Materials Nanoarchitectonics (MANA), and [‡]Advanced Nano Materials Laboratory (ANML), National Institute for Materials Science (NIMS), 1-1 Namiki, Tsukuba, Ibaraki 305-0044, Japan

[§]Magnetic Materials Center (MMC), NIMS, Sengen 1-2-1, Tsukuba, Ibaraki 305-0047, Japan

Supporting Information

ABSTRACT: $LiNbO_3$ (*LN*), corundum (*cor*), and hexagonal (*hex*) phases of $(In_{1-x}M_x)MO_3$ (x = 0.143; M = $Fe_{0.5}Mn_{0.5}$) were prepared. Their crystal structures were investigated with synchrotron X-ray powder diffraction, and their properties were studied by differential thermal analysis, magnetic measurements, and Mössbauer spectroscopy. The *LN*-phase was prepared at high pressure of 6 GPa and 1770 K; it crystallizes in space group *R*3*c* with a = 5.25054(7) Å, c = 13.96084(17) Å, and has a long-range antiferromagnetic ordering near T_N = 270 K. The *cor*- and *hex*-phases were obtained at ambient pressure by heating the *LN*-phase in air up to 870 and 1220 K, respectively. The *cor*-phase crystallizes in space group *R*-3*c* with a = 5.25047(10) Å, c = 14.0750(2) Å, and the *hex*-phase in space group $P6_3/mmc$ with a = 3.34340(18) Å, c = 11.8734(5) Å. T_N of the *cor*-phase is about 200 K, and T_N of the *hex*-phase is about 140 K. During irreversible transformations of *LN*-$(In_{1-x}M_x)MO_3$ with the (partial) cation ordering, the In^{3+}, Mn^{3+}, and Fe^{3+} cations become completely disordered in one crystallographic site of the corundum structure, and then they are (partially) ordered again in the *hex*-phase. *LN*-$(In_{1-x}M_x)MO_3$ exhibits a reversible transformation to a perovskite $GdFeO_3$-type structure (space group *Pnma*; a = 5.2946(3) Å, b = 7.5339(4) Å, c = 5.0739(2) Å at 10.3 GPa) at room temperature and pressure of about 5 GPa.

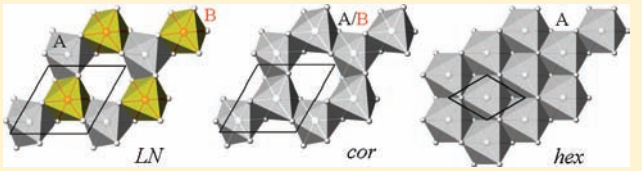

1. INTRODUCTION

ABO_3 compounds crystallize in a number of structure types, for example, perovskite, $LiNbO_3$, hexagonal $LuMnO_3$-type, hexagonal $BaMnO_3$-type, pyroxene, corundum, ilmenite (ordered corundum), rare earth sesquioxide structures (A, B, and C (bixbyite)), $PbReO_3$, $KSbO_3$, $AlFeO_3$, $CaIrO_3$, and others (Figure 1).[1] The $LiNbO_3$ structure, in principle, can be described as a highly distorted perovskite structure, to which it can be related by a displacive transformation.[2] The $LiNbO_3$ structure is often considered as a distinct structure type from perovskites because small A cations have octahedral 6-fold coordination instead of a 7−12-fold coordination in perovskites. From this point of view, $BiFeO_3$ is close to the $LiNbO_3$-type structure because six Bi−O distances (2.27 Å × 3 and 2.53 Å × 3) are much smaller than the other six Bi−O distances (3.22 Å × 3 and 3.44 Å × 3). Nevertheless, $BiFeO_3$ is always referred to as a perovskite because the BiO_6 polyhedron is highly distorted from an octahedral one.[3]

Some ABO_3 compounds with almost the same composition can have a few principally different modifications.[1,2] For example, $YMnO_3$ prepared at ambient pressure has a hexagonal $LuMnO_3$-type structure (space group $P6_3cm$; $a \approx 6.0$ Å, $c \approx 11.4$ Å); treatment at high pressure and temperature stabilizes a perovskite $GdFeO_3$-type modification at ambient conditions.[4] In_2O_3 is known in the bixbyite and corundum modifications at ambient conditions.[5] The perovskite-type modifications of stoichiometric $BaTiO_3$ (with corner-shared TiO_6 octahedra) transform to a hexagonal modification in $BaTiO_{3-\delta}$, where two TiO_6 octahedra are connected by a face.[6] Only a limited number of ABO_3 compounds have more than two principally different modifications stable at or quenchable to ambient conditions. For example, pyroxene, garnet-type, ilmenite, and perovskite modifications of $MgSiO_3$ are known.[2] Note that at high pressure and temperature, more unquenchable modifications can be found. For example, $MgSiO_3$ has a $CaIrO_3$-type phase (the so-called postperovskite phase),[2] and In_2O_3 has Rh_2O_3(II)-type and α-Gd_2S_3-type phases.[7,8] Pressure and temperature-induced phase transitions in ABO_3 are of great interest in materials science and earth science. Doped In_2O_3-based materials have been investigated a lot as transparent conducting oxides and diluted room-temperature ferromagnetic semiconductors.[5,9]

Recently, we have succeeded in preparation of the $LiNbO_3$-type (*LN*) phase of $(In_{1-x}M_x)MO_3$ ($x \approx 0.111-0.176$; M = $Fe_{0.5}Mn_{0.5}$) using a high-pressure synthetic method.[10] This phase has long-range antiferromagnetic ordering near room temperature and is a promising multiferroic material.[11,12] In this work, we report on the preparation and properties of corundum (*cor*) and hexagonal (*hex*) $YAlO_3$-type (space group $P6_3/mmc$; $a \approx 3.3$ Å, $c \approx 11.9$ Å) polymorphs of $(In_{1-x}M_x)MO_3$ (x = 0.143; M = $Fe_{0.5}Mn_{0.5}$).

Received: February 2, 2011
Published: May 23, 2011

dx.doi.org/10.1021/ja2010362 | J. Am. Chem. Soc. 2011, 133, 9405–9412

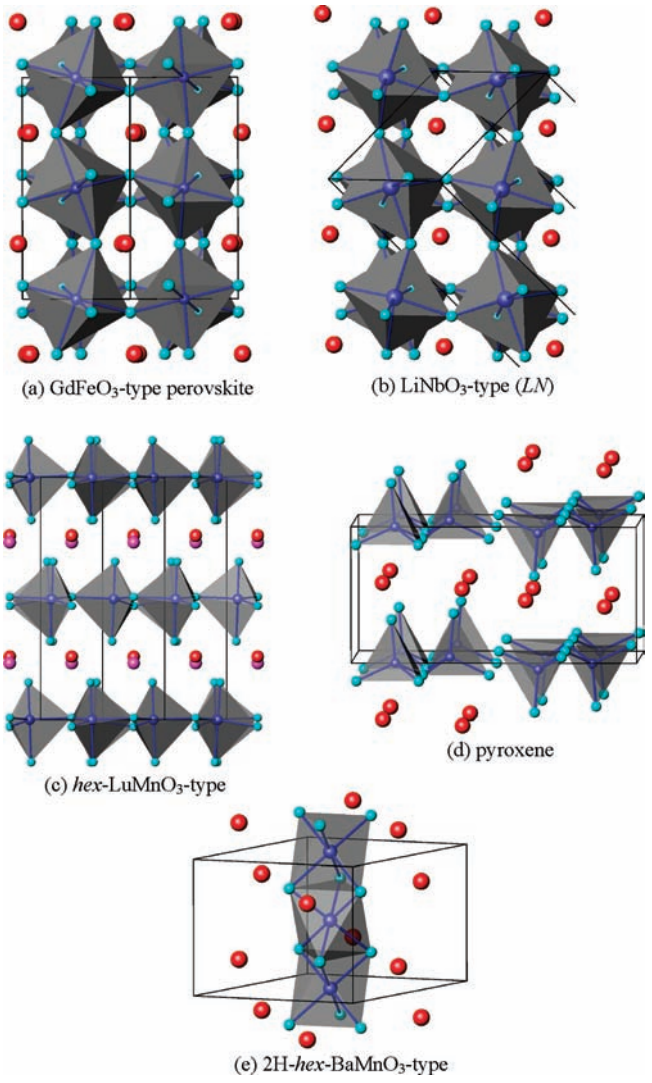

Figure 1. Polyhedral BO_n presentation of selected structure types in which ABO_3 compounds crystallize. A atoms are shown by red/pink spheres, oxygen atoms by cyan, and B atoms by blue. (a) $GdFeO_3$-type perovskite structure with corner-shared BO_6 octahedra exemplified by *perovskite*-$(In_{1-x}M_x)MO_3$. (b) $LiNbO_3$-type structure with BO_6 octahedra exemplified by *LN*-$(In_{1-x}M_x)MO_3$. (c) *hex*-$LuMnO_3$-type structure with BO_5 trigonal bipyramids exemplified by $InMnO_3$. (d) Pyroxene-type structure with BO_4 tetrahedra exemplified by KVO_3. (e) *hex*-$BaMnO_3$-type structure with face-shared BO_6 octahedra exemplified by 2H-$BaMnO_3$.

The *LN*-phase can be prepared at high pressure. The *cor*- and *hex*-modifications can be obtained at ambient pressure but only from the *LN*-phase. The irreversible transformation sequence of $LiNbO_3$ > corundum > hexagonal on heating at ambient pressure is a new one and of interest because it has the order—disorder—order character. At high pressure and room temperature, the *LN*-phase reversibly transforms to the perovskite $GdFeO_3$-type structure.

2. EXPERIMENTAL SECTION

2.1. Synthesis. *LN*-$(In_{1-x}M_x)MO_3$ (x = 0.143; M = $Fe_{0.5}Mn_{0.5}$) was prepared from stoichiometric mixtures of In_2O_3 (99.99%), Mn_2O_3 (99.99%), and Fe_2O_3 (99.999%) in a belt-type high pressure apparatus at 6 GPa and 1773 K for 30 min in Pt capsules.[10] After heat treatment, the sample was quenched to room temperature, and the pressure was slowly released. Differential thermal analysis (DTA) of the *LN*-phase showed one endothermal peak near 700 K and one exothermal peak near 1130 K on heating and no anomalies on cooling indicating irreversible phase transformations (see the Supporting Information). The *cor*-phase was obtained by heating the *LN*-phase to 870 K in a DTA experiment, and the *hex*-phase was obtained by heating the *LN*-phase to 1220 K in another DTA experiment. Note that a stoichiometric mixture of In_2O_3, Fe_2O_3, and Mn_2O_3 treated in air at 1170 K for 3 h was just a mixture of the initial oxides. The *hex*-phase appeared after the ambient pressure synthesis at 1270—1370 K. However, despite many attempts, the *hex*-phase could not be prepared in a single-phase form by the solid-state synthesis from oxides at ambient pressure (see the Supporting Information).

We note that initially the stoichiometry of the samples was written as $In_{1-y}Fe_{0.5}Mn_{0.5}O_{3-1.5y}$. The composition under the study with $x \approx 0.143$ corresponds to y = 0.25. Results similar to those reported in this Article were obtained for y = 0.2 ($x \approx 0.111$) and 0.3 ($x \approx 0.176$). We also tried to vary the Fe:Mn ratio for y = 0.25, $In_{1-y}Fe_{1-z}Mn_zO_{3-1.5y}$. In the Fe-rich side (e.g., z = 0.2), a corundum phase is stabilized under the above high-pressure high-temperature conditions similar to $InFeO_3$ with the corundum structure.[13] In the Mn-rich side (e.g., z = 0.8), a perovksite phase is stabilized similar to $(In_{1-x}Mn_x)MnO_3$.[14]

2.2. X-ray Powder Diffraction (XRD) and Physical Properties. Room-temperature laboratory XRD data were collected on a RIGAKU Ultima III diffractometer using Cu K_α radiation (40 kV, 40 mA, 2θ range of 10—120°, a step width of 0.02°, and a counting time of 10 s/step). High-temperature laboratory XRD data were collected on a RIGAKU RINT-TTR3 diffractometer using Cu K_α radiation (50 kV, 300 mA, 2θ range of 12—74°, a step width of 0.02°, and a counting time of 1 s/step) up to 1273 K with a step of 50 K in a vacuum of about 0.03 Pa. Synchrotron XRD data were collected at different temperatures (up to 823 K) on a large Debye—Scherrer camera at the BL02B2 beamline of SPring-8.[15] High-temperature synchrotron XRD data were measured during 3 min at each temperature point with the heating time of about 2 min between the points; heating was done by an N_2 gas flow system. The incident beam from a bending magnet was monochromatized to λ = 0.42328 Å. The samples were contained in (boro)glass capillary tubes with an inner diameter of 0.2 mm, and the capillary tubes were rotated during measurements. The synchrotron XRD data were collected by an imaging plate in a 2θ range from 2° to 75° with a step interval of 0.01°. Laboratory and synchrotron XRD data were analyzed by the Rietveld method with RIETAN-2000 software.[16]

Coefficients for analytical approximation to atomic scattering factors for In, Fe, Mn, and O were taken from ref 17. The pseudo-Voigt function of Toraya was used as a profile function.[18] The background was represented by an 11th-order Legendre polynomial. Isotropic atomic displacement parameters, B, with the isotropic Debye—Waller factor represented as $\exp((-B \sin^2 \theta)/\lambda^2)$ were assigned to all of the sites. Other experimental and refinement details are summarized in Table 1.

A symmetric diamond anvil cell (DAC), equipped with a culet diameter of 0.4 mm, was used for the room-temperature high-pressure synchrotron XRD experiments. The powder sample was put into a chamber (0.15 mm in diameter) in a rhenium gasket (0.8 mm in thickness) with a few small grains of ruby (less than 5 μm) to measure pressure.[19] The sample was immersed in a pressure medium (methanol:ethanol:water = 16:3:1) to present a hydrostatic condition. The in situ synchrotron XRD experiments were performed at the BL04B2 beamline of SPring-8.[20] A monochromatic X-ray beam (38 keV) was focused and collimated to the sample within 50 μm size. A diffracted X-ray beam was detected by an imaging plate in a 2θ range of 3.2—16.7°. Typical exposure time was 10 min. Diffraction patterns were collected with increasing pressure up to 10.3 GPa at intervals of 1—2 GPa. After that, the patterns in the decompression

dx.doi.org/10.1021/ja2010362 |J. Am. Chem. Soc. 2011, 133, 9405–9412

Table 1. Experimental and Refinement Details of $(In_{1-x}M_x)MO_3$ ($x = 0.143$; M = $Fe_{0.5}Mn_{0.5}$)

	LN-phase	*cor*-phase	*hex*-phase	*perovskite*-phase
conditions of data collection	293 K, AP[a]	293 K, AP	293 K, AP	293 K, 10.3 GPa
radiation	synchrotron	synchrotron	synchrotron	synchrotron
λ (Å)	0.42328	0.42328	0.42328	0.32779
2θ range used (deg)	4−48	5−48	2−48	3.2−16.7
step (deg)	0.01	0.01	0.01	∼0.01
number of refined parameters:				
lattice (a, b, c)	2	2	2	3
(x, y, z, B)	8	4	6	7
profile parameters	6	6	6	2
zero-shift	1	1	1	1
background	12	12	12	12
space group (No.)	*R*3*c* (161)	*R*-3*c* (167)	$P6_3/mmc$ (194)	*Pnma* (62)
Z	6	6	2	4
a (Å)	5.25054(7)	5.25047(10)	3.34340(18)	5.2946(3)
b (Å)				7.5339(4)
c (Å)	13.96084(17)	14.0750(2)	11.8734(5)	5.0739(2)
V (Å^3)	333.312(8)	336.028(11)	114.943(10)	202.39(2)
R_{wp} (%)	0.78	0.86	0.77	2.09
R_p (%)	0.52	0.56	0.55	1.43
R_I (%)	1.45	4.06	2.28	3.39
R_F (%)	1.17	2.60	1.64	2.14

[a] AP: ambient pressure.

process were taken. The sample submitted for the DAC experiments contained a small amount of the InOOH impurity.

Magnetic susceptibilities, $\chi = M/H$, were measured on a SQUID magnetometer (Quantum Design, MPMS) between 2 and 400 K in applied fields of 100 Oe, 1 kOe, and 10 kOe under both zero-field-cooled (ZFC) and field-cooled (FC; on cooling) conditions. Isothermal magnetization measurements were performed at 5 and 300 K between −50 and 50 kOe. ^{57}Fe Mössbauer spectra were measured with transmission geometry using a ^{57}Co/Rh source. The sample weight for the Mössbauer measurements was about 50 mg, and the sample thickness was about 10 μm. Obtained spectra were calibrated by α-Fe as a standard and were fitted by the Lorentzian function.

The DTA experiments were performed on a SII Exstar 6000 (TG-DTA 6200) system between 300 and 1270 K at a heating/cooling rate of 10 K/min in an Al_2O_3 holder.

3. RESULTS

3.1. Crystal Structure Analysis of the *LN*-, *cor*-, and *hex*-Phases. XRD patterns of the *LN*- and *cor*-phases are very similar to each other. Therefore, these phases could be distinguished only by the Rietveld analysis. In the case of the *LN*-phase, we tried different structural models including corundum-type (*R*-3*c*), ilmenite-type (*R*-3), and centrosymmetric perovskite-type (*R*-3*c*). However, all of these models gave poor matching between observed and calculated intensities for some reflections. Only the polar perovskite or $LiNbO_3$ model (*R*3*c*; with all sites fully occupied) gave excellent agreement between the observed and calculated synchrotron XRD patterns. In the case of the *cor*-phase, the best fit was obtained in the corundum structural model. The corundum structure has one cation site. Therefore, this site was supposed to be occupied by a virtual atom, M-*cor* = $In_{0.4445}Mn_{0.27775}Fe_{0.27775}$. All of the observed reflections of the *hex*-phase can be indexed in a hexagonal lattice with $a = 3.343$ Å, $c = 11.873$ Å. Reflection conditions give the $P6_3/mmc$ space group as a maximum space group. The crystal structure of the *hex*-phase was refined in this space group using the fractional coordinates of $InFeO_3$ (the ambient pressure modification) as the initial ones.[21] Two extreme models are possible for the *LN*- and *hex*-phases: an A-site- and oxygen-deficient $In_{0.75}(Mn_{0.5}Fe_{0.5})O_{2.625}$ model and a fully occupied $(In_{1-x}M_x)MO_3$ ($x = 0.143$; M = $Fe_{0.5}Mn_{0.5}$) model. For the *LN*- and *hex*-phases, we started from the deficient model. However, during refinements, we ended up with the fully occupied model. Because In^{3+} and (Fe^{3+},Mn^{3+}) ions have different ionic radii, we adopted a model where these ions are split at the A sites. Final lattice parameter and *R* factors of the *LN*-, *cor*-, and *hex*-phases at room temperature are listed in Table 1, and fractional coordinates and *B* parameters are in Table 2. Observed, calculated, and difference synchrotron XRD patterns are given in Figures 2 and 3.

3.2. Magnetic Properties of the *LN*-, *cor*-, and *hex*-Phases. Temperature-dependent magnetic susceptibilities of the *cor*- and *hex*-phases showed no anomalies (see the Supporting Information). Therefore, we used Mössbauer spectroscopy to get inside their magnetic properties. In the *hex*-phase, a long-range magnetic ordering takes place between 120 and 160 K (Figure 4a). Mössbauer spectra of the *cor*-phase revealed that a long-range ordering develops below about 200 K (Figure 4b). Mössbauer spectra of the *LN*-, *cor*-, and *hex*-phases at room temperature are shown in Figure 5 together with the fitting results. In the *LN*- and *cor*-phases, one paramagnetic doublet is seen. The *hex*-phase exhibits two paramagnetic doublets. The *LN*-phase also shows a contribution from a very smeared sextet because T_N is close to room temperature.[10] Isothermal magnetization curves (M vs H) of the *cor*-phase at 5 K show a very small hysteresis probably due to spin canting; almost no hysteresis was found in the *hex*-phase at 5 K (see the Supporting Information).

dx.doi.org/10.1021/ja2010362 |*J. Am. Chem. Soc.* 2011, 133, 9405–9412

Table 2. Structure Parameters of Different Modifications of $(In_{1-x}M_x)MO_3$ (x = 0.143; M = $Fe_{0.5}Mn_{0.5}$) at Room Temperature[a]

site	g	x	y	z	B (Å^2)
			$LiNbO_3$-type		
In	0.8571	0	0	0	0.54(2)
M1	0.1429	0	0	0.0208(8)	=B(In)
M2	1	0	0	0.21789(7)	0.12(3)
O	1	0.6341(6)	0.0172(4)	0.9539(3)	0.29(5)
			Corundum-type		
M-*cor*	1	0	0	0.35719(3)	0.87(2)
O	1	0.2993(4)	0	0.25	0.95(6)
			Hexagonal $YAlO_3$-type		
In	0.8571	0	0	0	0.605(15)
M1	0.0714	0	0	0.0104(15)	=B(In)
M2	1	1/3	2/3	1/4	0.13(2)
O1	1	0	0	1/4	0.79(6)
O2	1	1/3	2/3	0.08509(15)	0.67(5)
			Perovskite at 10.3 GPa		
In	0.8571	0.0543(4)	0.25	0.9836(8)	0.5[b]
M1	0.1429	0.0543(4)	0.25	0.9836(8)	0.5[b]
M2	1	0	0	0	0.5[b]
O1	1	0.429(4)	0.25	0.112(3)	0.5[b]
O2	1	0.320(3)	0.0609(18)	0.678(2)	0.5[b]

[a] M1 = M2 = $Mn_{0.5}Fe_{0.5}$; M-*cor* = $In_{0.4445}Mn_{0.27775}Fe_{0.27775}$. g is the occupation factor, and B is the isotropic thermal parameter. [b] Fixed values.

Magnetic susceptibilities of the *LN*-phase demonstrate a small bump or increase near room temperature on cooling (see the Supporting Information). Its origin may come from the development of a weak ferromagnetic component below T_N due to spin canting. The M versus H curves of the *LN*-phase confirmed weak ferromagnetic properties below T_N.[10] We note that $BiFeO_3$ also shows an increase of magnetic susceptibilities at T_N = 643 K on cooling[22] even though it is a pure antiferromagnet (due to cycloidal rotation of canted antiferromagnetic spins giving rise to a zero net moment).[3]

The inverse magnetic susceptibilities in the high-temperature region were fit by the Curie−Weiss equation:

$$\chi(T) = \chi_0 + \mu_{eff}^2 N(3k_B(T-\theta))^{-1} \quad (1)$$

where χ_0 is temperature-independent contributions, μ_{eff} is effective magnetic moment, N is Avogadro's number, k_B is Boltzmann's constant, and θ is the Curie−Weiss constant. The values obtained are μ_{eff} = 5.21(1)μ_B and θ = −512(3) K for the *LN*-phase, μ_{eff} = 5.35(1)μ_B and θ = −506(2) K for the *cor*-phase, and μ_{eff} = 5.08(2)μ_B and θ = −802(8) K for the *hex*-phase. The μ_{eff} values are close the expected value of 5.43 μ_B, confirming the oxidation states of Fe^{3+} and Mn^{3+}. The large negative θ values show strong antiferromagnetic coupling between magnetic ions. The θ value of −802(8) K for the *hex*-phase is close to that of *hex*-$InMnO_3$ ($\theta \approx -770$ K).[23]

3.3. Phase Transitions at High Pressure and the Crystal Structure of the Perovskite Phase. Figure 6 demonstrates that *LN*-$(In_{1-x}M_x)MO_3$ (x = 0.143; M = $Fe_{0.5}Mn_{0.5}$) transforms to a perovskite $GdFeO_3$-type structure at room temperature and high pressure. The transformation starts from about 5 GPa on compression. This phase transition is reversible: on decompression, the *LN*-phase appears below about 2 GPa. The structure parameters at 10.3 GPa were refined, and they are given in Tables 1 and 2. Figure 6b shows the Rietveld refinement fits. Because the quality of the synchrotron XRD data at high-pressure is lower and the 2θ range is limited, the thermal displacement parameters were fixed for all of the atoms, and the In and M1 atoms at the A site were not split.

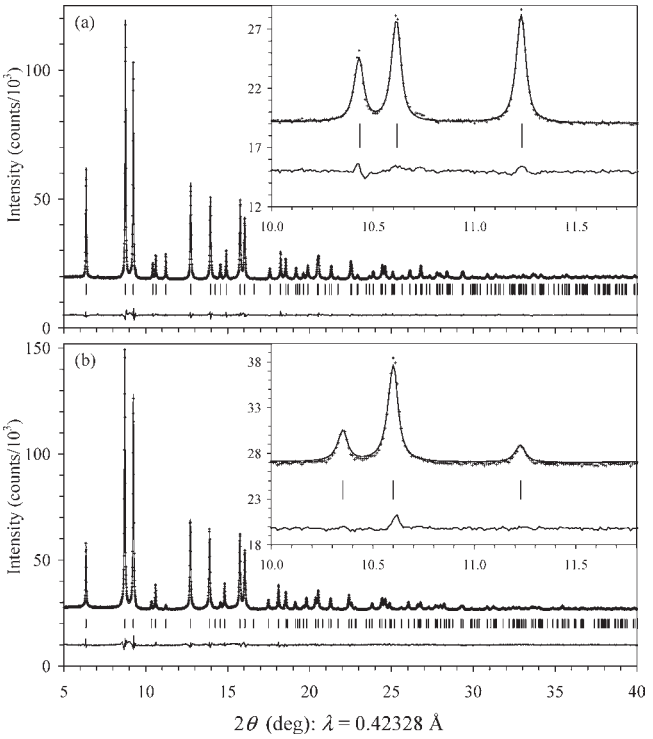

Figure 2. Portions of experimental (+), calculated (−), and difference synchrotron (λ = 0.42328 Å) X-ray powder diffraction patterns for (a) *LN*-$(In_{1-x}M_x)MO_3$ (x = 0.143; M = $Fe_{0.5}Mn_{0.5}$) and (b) *cor*-$(In_{0.889}Mn_{0.5555}Fe_{0.5555})O_3$ at room temperature. Bragg reflections are indicated by tick marks. Insets show enlarged details of the fittings.

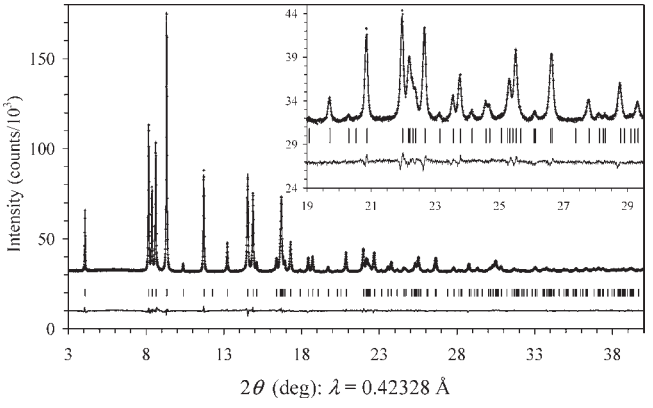

Figure 3. Portions of experimental (+), calculated (−), and difference synchrotron (λ = 0.42328 Å) X-ray powder diffraction patterns for *hex*-$(In_{1-x}M_x)MO_3$ (x = 0.143; M = $Fe_{0.5}Mn_{0.5}$) at room temperature. Bragg reflections are indicated by tick marks. Inset shows enlarged details of the fitting.

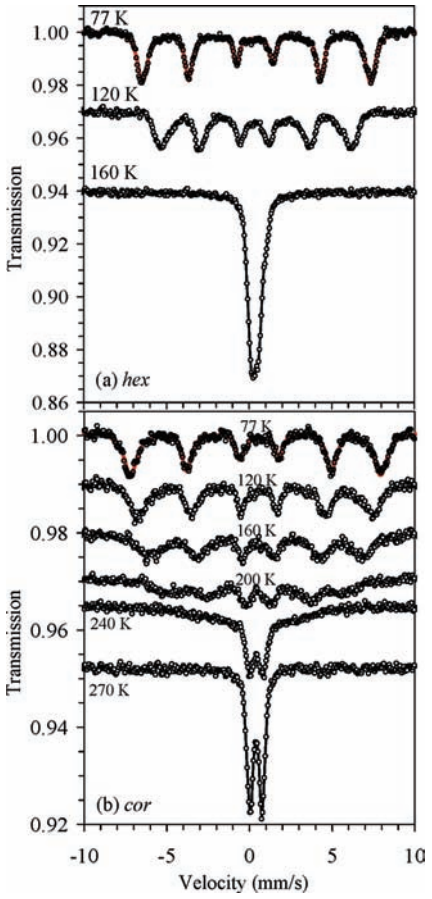

Figure 4. Mössbauer spectra of (a) *hex*-$(In_{1-x}M_x)MO_3$ (x = 0.143; M = $Fe_{0.5}Mn_{0.5}$) and (b) *cor*-$(In_{0.889}Mn_{0.5555}Fe_{0.5555})O_3$ at low temperatures. The "○" are experimental data; the lines are drawn for eye (except for 77 K). The lines at 77 K are the fitting results (*hex*, IS = 0.389(8) mm/s, ε = 0.057(8) mm/s, H = 427.6(6) kOe; *cor*, IS = 0.479(13) mm/s, ε = −0.108(13) mm/s, H = 469(1) kOe, where IS is the isomer shift, ε is the quadruple shift, and H is the hyperfine field).

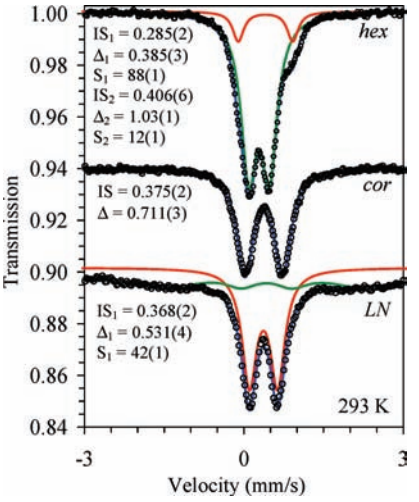

Figure 5. Mössbauer spectra of *hex*-, *cor*-, and *LN*-phases of $(In_{1-x}M_x)MO_3$ (x = 0.143; M = $Fe_{0.5}Mn_{0.5}$) at room temperature. The "○" are experimental data; the lines are the fits. The fitting parameters are given on the figure, where IS is the isomer shift (mm/s), Δ is the quadruple splitting (mm/s), and S is the area (%).

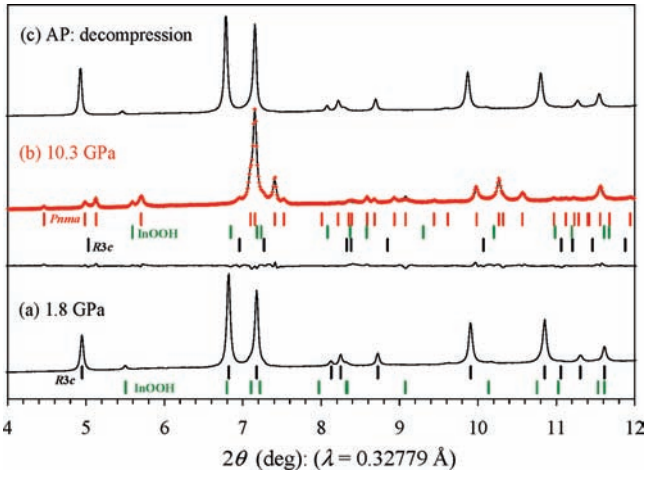

Figure 6. (a,c) Portions of experimental synchrotron (λ = 0.32779 Å) X-ray powder diffraction patterns (lines) of *LN*-$(In_{1-x}M_x)MO_3$ (x = 0.143; M = $Fe_{0.5}Mn_{0.5}$) at room temperature and 1.8 GPa (on compression) and at ambient pressure (AP) after decompression. Bragg reflections are indicated by tick marks for the *LN*-phase (*R*3*c*) and the InOOH impurity (the second green row of Bragg reflections at 1.8 GPa). (b) Portions of experimental (+), calculated (−), and difference synchrotron (λ = 0.32779 Å) X-ray powder diffraction patterns for *perovskite*-$(In_{1-x}M_x)MO_3$ (x = 0.143; M = $Fe_{0.5}Mn_{0.5}$) at room temperature and 10.3 GPa. Bragg reflections are indicated by tick marks for the *perovskite*-phase (*Pnma*), the InOOH impurity, and the remaining traces of the *LN*-phase.

4. DISCUSSION

A and B cations are ordered in the $LiNbO_3$-type structure (Figures 7 and 8). In the case of *LN*-$(In_{1-x}M_x)MO_3$ (x = 0.143; M = $Fe_{0.5}Mn_{0.5}$), the B site is occupied by $Fe_{0.5}Mn_{0.5}$, and the A site is occupied by $In_{0.857}Fe_{0.07}Mn_{0.07}$. It is impossible to distinguish between Fe^{3+} and Mn^{3+} ions with X-rays. Therefore, random distribution of these ions was assumed. Because both sites are octahedral and the amount of Fe^{3+} at the A site is small, the Mössbauer spectrum of *LN*-$(In_{1-x}M_x)MO_3$ at room temperature shows only one doublet.

On heating at ambient pressure, *LN*-$(In_{1-x}M_x)MO_3$ transforms first to the *cor*-phase. This transformation is endothermal, indicating that it corresponds to a transition from one metastable phase to another metastable phase. Because of a noticeable DTA effect, it should be the first-order transition. The corundum structure has hexagonal closed-packed oxygen atoms with cations filling two-thirds of the formed octadedral sites. In one octahedral layer perpendicular to the c axis of this structure, there are alternating two filled octahedra and one empty octahedron (Figure 8). The transformation from the *LN*-phase to the *cor*-phase can be described as disordering of all In^{3+}, Mn^{3+}, and Fe^{3+} cations between the filled octahedral sites. The corundum structure has one crystallographycally independent cation site. Therefore, the Mössbauer spectrum of *cor*-phase at room temperature shows only one doublet. It is interesting to note that in the corundum-type solid solutions $In_{2-2x}Zn_xSn_xO_3$ local ordering of Zn and Sn atoms was found by EXAFS studies, but the average structure is of the corundum-type with complete disordering.[9] A transformation from the corundum (or ilmenite) structure to the $LiNbO_3$ structure occurs at high pressure and high temperature in some oxides, for example, $FeTiO_3$, with the quenchable *LN*-phase.[2,24]

dx.doi.org/10.1021/ja2010362 |J. Am. Chem. Soc. 2011, 133, 9405–9412

A back-transformation (that is, from an *LN*-phase to a *cor*-phase) occurs on heating at ambient pressure in $FeTiO_3$.[24] In our work, we observed a similar transformation in *LN*-$(In_{1-x}M_x)MO_3$. However, we found no evidence for the ordered corundum structure in *cor*-$(In_{1-x}M_x)MO_3$.

On further heating at ambient pressure, the *cor*-phase transforms to the *hex*-phase. This transformation is strongly exothermal, indicating that it corresponds to a transition from a metastable phase (with excess energy) to a thermodynamically stable phase. The *hex*-polymorph is isostructural with $InFeO_3$ (the *hex*-$YAlO_3$-type structure),[21,25] with the high-temperature centrosymmetric form of $YMnO_3$,[26] and with $YMnO_{2.80}$.[26] The $YAlO_3$-type structure (space group $P6_3/mmc$; $a \approx 3.7$ Å, $c \approx 10.5$ Å) can be distinguished from the ferroelectric $LuMnO_3$-type structure (space group $P6_3cm$; $a \approx 6.0$ Å, $c \approx 11.4$ Å) by the cell dimensions. The *hex*-phase can be described as alternating layers of octahedra and trigonal bipyramids. The A site is occupied by $(In_{0.857}Fe_{0.07}Mn_{0.07})$ similar to the *LN*-$(In_{1-x}M_x)MO_3$ (taking into account that Fe^{3+} and Mn^{3+} ions are undistinguishable with X-rays). The A cations are located in the octahedral holes of close-packed O2 layers. As compared to the $LiNbO_3$ and corundum structures, all of the octahedral holes are filled in the layer (Figure 8). Therefore, (partial) ordering of In^{3+}, Mn^{3+}, and Fe^{3+} cations take place again in the *hex*-phase.

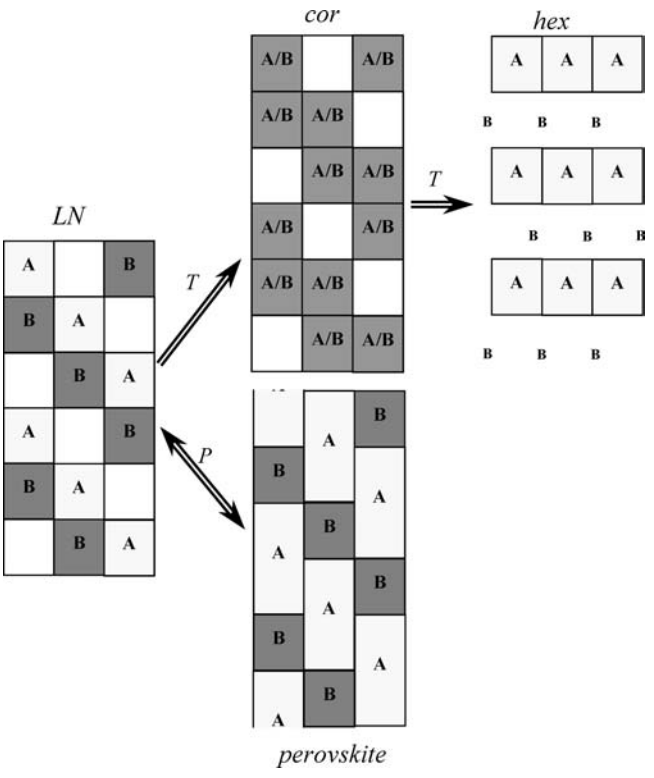

Figure 7. Schematic illustration of cation ordering in ABO_3-type structures:[9] the $LiNbO_3$ (*LN*), corundum (*cor*), hexagonal (*hex*), and perovskite structures. Squares represent octahedra (empty squares are vacant octahedra). Arrows show the pressure-induced reversible and temperature-induced irreversible transformations in $(In_{1-x}M_x)MO_3$ ($x = 0.143$; $M = Fe_{0.5}Mn_{0.5}$).

The *hex*-phase exhibits two doublets in the Mössbauer spectrum at room temperature. These data confirm the conclusion of the structural analysis that all cation sites in *hex*-$(In_{1-x}M_x)MO_3$ are fully occupied with the majority of Fe^{3+} located in the trigonal bipyramidal coordination and the minority of Fe^{3+} located in the octahedral A-type site. The isomer shift and quadruple splitting of Fe^{3+} in the trigonal bipyramidal coordination are different from those of Fe^{3+} in the octahedral coordination (Figure 5). The experimental ratio of 12(1):88(1) between the areas of the two doublets is in excellent agreement with the expected ratio of 12.3:87.7 for *hex*-$(In_{0.857}Fe_{0.07}Mn_{0.07})(Fe_{0.5}Mn_{0.5})O_3$.

It is interesting to note that at 1130 K, where the corundum-to-hexagonal transformation takes place according to the DTA, no reaction was observed between mixtures of oxide precursors. Oxide precursors react at higher temperatures to form the *hex*-phase. Yet we could not obtain the bulk *hex*-phase in a single-phase form similar to $InFeO_3$.[27] In the case of $InFeO_3$, this peculiarity was explained, assuming that the decomposition temperature is very close to the synthesis temperature. Therefore, the "low-temperature" (that is, below the decomposition temperature) transformation from the *cor*-phase to the *hex*-phase seems to be the only way to prepare the bulk *hex*-phase in a single-phase form.

The magnetization measurements coupled with the Mössbauer spectroscopy data indicate that long-range antiferromagnetic ordering takes place in all of the polymorphs (stable at ambient conditions). The long-range magnetic ordering in *hex*-$(In_{1-x}M_x)MO_3$ ($x = 0.143$; $M = Fe_{0.5}Mn_{0.5}$) occurs at about 140 K. This temperature is close to $T_N = 118$ K of the hexagonal $InMnO_3$.[23,28] Unfortunately, no information is available about T_N of the hexagonal $InFeO_3$.[27,29]

At room temperature and pressure of about 5 GPa, *LN*-$(In_{1-x}M_x)MO_3$ reversibly transforms to the $GdFeO_3$-type perovskite structure (Figure 6). This kind of transformation is often observed in the $LiNbO_3$-type oxides.[2,30] It occurs reversibly at room temperature because it involves movements of A-type cations inside their polyhedra and rotation of BO_6 octahedra (Figure 7).[2] High-pressure experiments performed at room temperature for the *cor*-phase showed no transformations up to 10.1 GPa. This fact also confirmed a different nature of the *LN*- and *cor*-phases despite their similar XRD patterns (Figure 2).

Table 3 summarizes the known $InBO_3$-type compounds and the structure types in which they crystallize. The unique character of

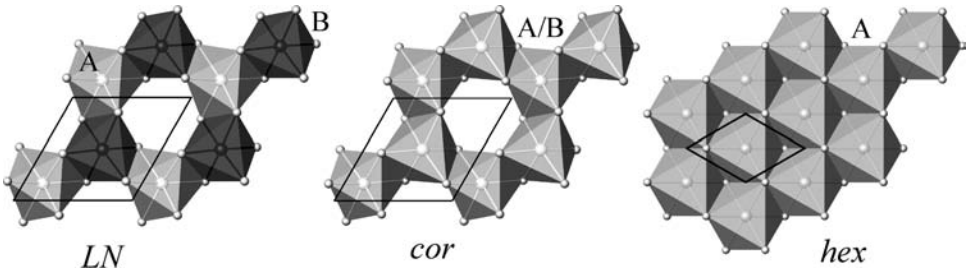

Figure 8. One layer (running perpendicular to the *c* axes) of octahedra in the $LiNbO_3$-type, corundum, and hexagonal structures.

dx.doi.org/10.1021/ja2010362 |*J. Am. Chem. Soc.* 2011, 133, 9405–9412

Table 3. Structural Variations of the $InBO_3$-type Compounds Stable at or Quenchable to Ambient Conditions[a]

compound	structural types
$InVO_3$	bixbyite (AP)[31]
$InCrO_3$	$GdFeO_3$-type perovskite (HP)[32]
$InMnO_3$	*hex*-$LuMnO_3$ (AP);[23,28] *hex*-$YAlO_3$ (AP)[25]
$(In_{1-x}Mn_x)MnO_3$	$GdFeO_3$-related perovskite (HP);[14] bixbyite (AP/HP)[14]
$InFeO_3$	*hex*-$YAlO_3$ (AP);[21,27] corundum (HP)[13]
$InScO_3$	corundum (HP)[13]
$InGaO_3$	β-Ga_2O_3 (AP);[33] *hex*-$YAlO_3$ (HP)[33]
$InRhO_3$	$GdFeO_3$-type perovskite (HP)[32]
$InInO_3$	bixbyite (AP);[5] corundum (HP)[5]
$(In_{1-x}M_x)MO_3$ (x = 0.143; M = $Fe_{0.5}Mn_{0.5}$)	$LiNbO_3$ (HP); corundum (AP/HP); *hex*-$YAlO_3$ (AP/HP) (this work)

[a] AP, a phase prepared at ambient pressure; HP, a phase prepared at high pressure (and high temperature) and quenched to ambient conditions; AP/HP, a phase prepared at ambient pressure but from the high-pressure modification.

$(In_{1-x}M_x)MO_3$ (x = 0.143; M = $Fe_{0.5}Mn_{0.5}$) can be seen. First, it is the only system where the $LiNbO_3$-type structure is formed so far. Second, it shows the maximum number of the structural variants for the same composition among $InBO_3$. Third, it demonstrates a unique sequence of phase transformations on heating at ambient pressure. A related system $(In_{1-x}Mn_x)MnO_3$ just shows a transformation from the perovskite-type structure to the bixbyite-type structure.[14]

In conclusion, we prepared three modifications of $(In_{1-x}M_x)MO_3$ (x = 0.143; M = $Fe_{0.5}Mn_{0.5}$), which are stable at ambient pressure, and observed one unquenchable modification at high pressure. Their crystal structures were investigated with synchrotron X-ray powder diffraction. All of them show long-range antiferromagneic ordering despite significant structural disorder. The irreversible transformation sequence of $LiNbO_3$ > corundum > hexagonal on heating at ambient pressure is a new one and of interest because it has the order−disorder−order character. The *cor*-to-*hex* transformation at low temperatures in $(In_{1-x}M_x)MO_3$ opens new ways for the stabilization of *hex*-$(In_{1-x}M_x)MO_3$.

■ ASSOCIATED CONTENT

Ⓢ Supporting Information. Details of DTA results, magnetization data, temperature dependence of the XRD patterns and intensities of some XRD reflections, details of the Mössbauer spectra of the *hex*-phase in the paramagnetic state, results of the ambient-pressure synthesis of $In_{0.75}Mn_{0.5}Fe_{0.5}O_{2.625}$, and bond lengths for all modifications. This material is available free of charge via the Internet at http://pubs.acs.org.

■ AUTHOR INFORMATION

Corresponding Author
alexei.belik@nims.go.jp

■ ACKNOWLEDGMENT

This work was supported by World Premier International Research Center Initiative (WPI Initiative, MEXT, Japan), the NIMS Individual-Type Competitive Research Grant, the Japan Society for the Promotion of Science (JSPS) through its "Funding Program for World-Leading Innovative R&D on Science and Technology (FIRST Program)", and the Grants-in-Aid for Scientific Research (22246083 and 22340164) from JSPS, Japan. The synchrotron radiation experiments were performed at the SPring-8 with the approval of the Japan Synchrotron Radiation Research Institute (Proposal Numbers: 2009A1136, 2010A1215, 2009B1172). We thank Drs. J. Kim, N. Tsuji, N. Hirao, and Y. Ohishi for their assistance at SPring-8 and Dr. Y. Yamabe-Miratai of NIMS for her help with the high-temperature laboratory XRD experiment.

■ REFERENCES

(1) (a) Giaquinta, D. M.; zur Loye, H.-C. *Chem. Mater.* **1994**, *6*, 365. (b) Bharathy, M.; Fox, A. H.; Mugavero, S. J.; zur Loye, H.-C. *Solid State Sci.* **2009**, *11*, 651.
(2) Navrotsky, A. *Chem. Mater.* **1998**, *10*, 2787.
(3) Catalan, G.; Scott, J. F. *Adv. Mater.* **2009**, *21*, 2463.
(4) Uusi-Esko, K.; Malm, J.; Imamura, N.; Yamauchi, H.; Karppinen, M. *Mater. Chem. Phys.* **2008**, *112*, 1029.
(5) Epifani, M.; Siciliano, P.; Gurlo, A.; Barsan, N.; Weimer, U. *J. Am. Chem. Soc.* **2004**, *126*, 4078.
(6) Kolodiazhnyi, T.; Belik, A. A.; Wimbush, S. C.; Haneda, H. *Phys. Rev. B* **2008**, *77*, 075103.
(7) Yusa, H.; Tsuchiya, T.; Sata, N.; Ohishi, Y. *Phys. Rev. B* **2008**, *77*, 064107.
(8) Yusa, H.; Tsuchiya, T.; Tsuchiya, J.; Sata, N.; Ohishi, Y. *Phys. Rev. B* **2008**, *78*, 092107.
(9) Hoel, C. A.; Amores, J. M. G.; Morn, E.; Alario-Franco, M. A.; Gaillard, J.-F.; Poeppelmeier, K. R. *J. Am. Chem. Soc.* **2010**, *132*, 16479.
(10) Belik, A. A.; Furubayashi, T.; Matsushita, Y.; Tanaka, M.; Hishita, S.; Takayama-Muromachi, E. *Angew. Chem., Int. Ed.* **2009**, *48*, 6117.
(11) Kan, E.; Xiang, H.; Lee, C.; Wu, F.; Yang, J.; Whangbo, M.-H. *Angew. Chem., Int. Ed.* **2010**, *49*, 1603.
(12) Alonso, J. A. *ChemPhysChem* **2010**, *11*, 58.
(13) (a) Shannon, R. D. *Solid State Commun.* **1966**, *4*, 629. (b) Prewitt, C. T.; Shannon, R. D.; Rogers, D. B.; Sleight, A. W. *Inorg. Chem.* **1969**, *8*, 1985.
(14) Belik, A. A.; Matsushita, Y.; Tanaka, M.; Takayama-Muromachi, E. *Angew. Chem., Int. Ed.* **2010**, *49*, 7723.
(15) Nishibori, E.; Takata, M.; Kato, K.; Sakata, M.; Kubota, Y.; Aoyagi, S.; Kuroiwa, Y.; Yamakata, M.; Ikeda, N. *Nucl. Instrum. Methods Phys. Res., Sect. A* **2001**, *467−468*, 1045.
(16) Izumi, F.; Ikeda, T. *Mater. Sci. Forum* **2000**, *321−324*, 198.
(17) *International Tables for Crystallography*, 2nd ed.; Wilson, A. J. C., Prince, E., Eds.; Kluwer: Dordrecht, The Netherlands, 1999; Vol. C, pp 572−574.
(18) Toraya, H. *J. Appl. Crystallogr.* **1990**, *23*, 485.
(19) Mao, H. K.; Xu, J.; Bell, P. M. *J. Geophys. Res.* **1986**, *91*, 4673.
(20) Kohara, S.; Itou, M.; Suzuya, K.; Inamura, Y.; Sakurai, Y.; Ohishi, Y.; Takata, M. *J. Phys.: Condens. Matter* **2007**, *19*, 506101.
(21) Giaquinta, D. M.; Davis, W. M.; zur Loye, H. C. *Acta Crystallogr., Sect. C* **1994**, *50*, 5.
(22) Roginskaya, Yu. E.; Venevtsev, Yu. N.; Fedotov, S. A.; Zhdanov, G. S. *Sov. Phys. Crystallogr.* **1964**, *8*, 490.
(23) Belik, A. A.; Kamba, S.; Savinov, M.; Nuzhnyy, D.; Tachibana, M.; Takayama-Muromachi, E.; Goian, V. *Phys. Rev. B* **2009**, *79*, 054411.
(24) Mehta, A.; Leinenweber, K.; Navrotsky, A.; Akaogi, M. *Phys. Chem. Miner.* **1994**, *21*, 207.
(25) Giaquinta, D. M.; zur Loye, H. C. *J. Am. Chem. Soc.* **1992**, *114*, 10952.
(26) Overton, A. J.; Best, J. L.; Saratovsky, I.; Hayward, M. A. *Chem. Mater.* **2009**, *21*, 4940.
(27) (a) Nodari, I.; Alebouyeh, A.; Brice, J. F.; Gerardin, R.; Evrard, O. *Mater. Res. Bull.* **1988**, *23*, 1039. (b) Gerardin, R.; Aqachmar, E. H.; Alebouyeh, A.; Evrard, O. *Mater. Res. Bull.* **1989**, *24*, 1417.

(28) Greedan, J. E.; Bieringer, M.; Britten, J. F.; Giaquinta, D. M.; zur Loye, H. C. *J. Solid State Chem.* **1995**, *116*, 118.
(29) Seki, M.; Konya, T.; Inaba, K.; Tabata, H. *Appl. Phys. Express* **2010**, *3*, 105801.
(30) (a) Yusa, H.; Akaogi, M.; Sata, N.; Kojitani, H.; Yamamoto, R.; Ohishi, Y. *Phys. Chem. Miner.* **2006**, *33*, 217. (b) Leinenweber, K.; Wang, Y.; Yagi, T.; Yusa, H. *Am. Mineral.* **1994**, *79*, 197.
(31) Lundgren, R. J.; Cranswick, L. M. D.; Bieringer, M. *J. Solid State Chem.* **2006**, *179*, 3599.
(32) Shannon, R. D. *Inorg. Chem.* **1967**, *6*, 1474.
(33) Shannon, R. D.; Prewitt, C. T. *J. Inorg. Nucl. Chem.* **1968**, *30*, 1389.